Control of an oscillating water column wave energy converter based on dielectric elastomer generator

Noname manuscript No.
(will be inserted by the editor)

Control of an Oscillating Water Column Wave Energy Converter Based on Dielectric Elastomer Generator

Gastone Pietro Rosati Papini · Giacomo Moretti · Rocco Vertechy · Marco Fontana

Received: date / Accepted: date

Abstract This paper introduces a model-based control strategy for a wave energy converter (WEC) based on dielectric elastomer generators (DEG), i.e. a device that can convert the energy of ocean waves into electricity by employing deformable elastomeric transducers with variable capacitance. The analysed system combines the concept of oscillating water column (OWC) WEC with an inflated circular diaphragm DEG (ICD-DEG). The device features strongly non-linear dynamics due to the ICD-DEG electro-hyperelastic response and the compressibility of the air volume comprised between the water column and the ICD-DEG, while the hydrodynamic loads can be approximated as linear. The optimal control solution that maximises the power extraction of the device is numerically investigated in the case of monochromatic waves over the typical frequency and amplitude ranges of sea-waves. The more realistic case of panchromatic waves is also analysed through the implementation, in simulation environment, of a real-time controller. This regulator is based on a simple sub-optimal control logic that is deduced from the monochromatic case. Performance of the proposed control strategy is illustrated in comparison with unoptimised algorithms.

Keywords Wave energy converter · oscillating water column · dielectric elastomer generator · optimal control

G. P. Rosati Papini, G. Moretti
Scuola Superiore Sant'Anna, P.za Dei Martiri 33, 56126 Pisa

Rocco Vertechy
University of Bologna, Viale Risorgimento 2, Bologna, Italy

M. Fontana
University of Trento,Via Sommarive 9, 38123 Trento, Italy
E-mail: marco.fontana-2@unitn.it

1 Introduction

The energy carried by ocean waves is considered a strategic resource of renewable energy for electricity production. Such an interest is generated by its great potential, wide geographical distribution and high predictability as well as good match between supply and demand [32]. However, although a lot of effort has been spent in the search of suitable solutions for wave energy converters (WECs) [10], this technology has not yet reached commercial maturity. This is due to different issues including technical and economic unfavourable factors. As for technical issues, the main complexities and problems are found in: the presence of highly corrosive ambient, that is incompatible with the metallic materials of structural components [21]; the relatively high ratios between peak and average loads; the complexity and relatively low reliability of components. In particular, a critical component of WECs that is strongly affected by the previously mentioned issues is the so-called power take off (PTO) unit, i.e. the subsystem that is responsible to convert mechanical energy into electricity.

Recently, a new class of energy converter based on soft elastomeric components has been proposed for the implementation of a new generation of WECs [33]. Specifically, dielectric elastomer generators (DEGs) have been identified as a promising technology due to their low cost, low weight, corrosion resistance, intrinsic oscillating nature of their working principle and type of their operation that is rather independent of the oscillation frequency. In the last decade, several research institutions and companies have started research programmes oriented to investigate solutions and methods for the development of such a kind of devices [6, 22, 29, 35].

Different concepts of DEG-based WEC have been proposed and among them a very promising system

is the polymeric oscillating water column (Poly-OWC) [36, 39]. The working principle of this WEC, illustrated in Fig. 1, is based on a collector that encloses a water column and an air volume. The column is put in reciprocating motion by wave-induced oscillating pressure exerted through a submerged aperture. This movement generates pressure variation inside an air chamber on top of the water column. Conventional oscillating water column (OWC) WECs, employ a turbo generator as the PTO. In the Poly-OWC concept, the PTO is implemented with an inflatable circular diaphragm DEG (ICD-DEG). The core component of such an energy converter is a highly deformable elastomeric membrane made of a stack of dielectric and conductive layers. These layers are arranged and connected to compose a large-scale variable/deformable capacitor. Compared to turbo generators, ICD-DEGs features greater architetural simplicity, as they do not have further moving parts but the polymeric layers and, according to preliminary techno-economic analyses, they might lead to an improvement in the levelised cost of energy produced by OWCs [36].

In Poly-OWC, the energy conversion takes place through the electrostatic generation principle, i.e./ through the instantaneous control of charge and voltage on the ICD-DEG electrodes while a variation in its capacitance is induced by the oscillating air-chamber pressure. Such a controller can be implemented according to different strategies that aim at maximizing the electrical power output of the device. The optimal activation profiles that have to be followed to maximize the performance of ICD-DEGs have been theoretically and experimentally studied [23, 24, 26], demonstrating their huge potential. However, the reported researches are focussed on quasi-static simulations or experiments in which the deformations are commanded by a position-controlled external mechanical input. Differently, in WEC applications the amount of electrical energy that can be generated over a period of time should consider a more general regulation strategy. Specifically, in order to maximise the fraction of wave power that is converted into electricity, the problem must be studied in a comprehensive way, i.e. the dynamic interaction between DEG and hydrodynamics has to be considered through a coupled model capable to capture the non-linearities intrinsically present in the Poly-OWC response (e.g., ICD-DEG electro-mechanical response, air chamber compressibility) and the regulation should be implemented with a more complex control of the electrical activation.

In this paper, we investigate the problem of controlling the Poly-OWC (see Fig. 1), with the aim of maximizing the producible electrical energy while operating within the constraints given by a set of physical limitations of the system. The proposed approach starts with the formulation of an optimisation procedure based on a discretisation of the system's dynamics equations. Such a solution is used to identify the optimal steady-state periodic dynamics that maximise the power output in the presence of monochromatic waves.

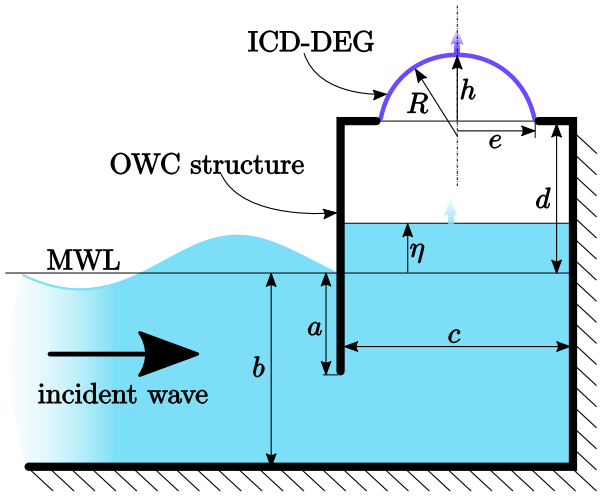

Fig. 1: Schematic of a Poly-OWC and definition of the relevant dimensions.

In a second phase, the more realistic case of real-time control for panchromatic waves is considered. WECs control in stochastic irregular waves is a relevant technical challenge. Optimal control strategies, which maximize the WEC power output in real-time, are non casual, and they thus require a prediction of the incident wave profiles and of the wave excitation force, as well as the online solution of an optimisation problem [7, 12]. Practical sub-optimal solutions might use prediction-free slow-adaptive controllers, based on slowly-varying control settings that are adjusted based on the spectral content of the incoming sea waves [17]. In our problem, the optimisation procedure that is employed for the monochromatic case results impractical for real-time controllers for operation in panchromatic waves, due to its high computational burden and the above mentioned need for prediction. Thus, a slow-adaptive control strategy for panchromatic waves is proposed, which is based on a simple logic that takes into account the results obtained by the study of the monochromatic wave case. The proposed control scheme uses the sole reading of a pressure sensor inside the OWC air chamber to regulate the electrical state of the DEG. Such solution is implemented and verified in simulation environment.

The paper is organized as follows. Section 2 illustrates the dynamic model of the device that integrates hydrodynamic and PTO sub-models; Sect. 3 introduces

the formulation of the optimal control problem; Sect. 4 shows the optimisation procedure results of a case study on a reference Poly-OWC and employs them to deduce a solution for real time control; Sect. 5 draws conclusions and proposes possible future works.

2 Dynamic modelling

This section illustrates the coupled model that is employed to formulate the optimisation problem and to implement simulations for the assessment of the proposed control logic. Such a model is based on previous work of some of the authors [30] and is composed of a hydrodynamic model of the OWC collector and a DEG-PTO electro-mechanical model, coupled through a simplified model for the air enclosed in the chamber. This modelling approach has been previously validated through wave-tank experiments and [31, 40]. The three sub-sections that follow illustrate these models and provide details on the underlying assumptions and hypotheses.

2.1 Hydrodynamic Model

The hydrodynamics of the OWC is modelled through a simplified approach by assuming potential flow and linear wave theory. The problem is reduced to just one single degree of freedom (DoF) through the so called "rigid piston" approximation, i.e. free surface of the water column remains perfectly flat and horizontal during the motion [12, 30]. Under this hypothesis the vertical displacement of the water inside the chamber can be described by the position η (positive for upward displacements). If viscous damping is neglected, the equation of dynamics reads as [3]:

$$m_\infty \ddot{\eta}(\tau) + \int_0^\tau k_r(\tau-\xi)\dot{\eta}(\xi)\mathrm{d}\xi + \rho_w g S \eta(\tau) = f_e(\tau) + f(\tau). \quad (1)$$

where:

- τ is time;
- $\dot{\eta}(\tau)$, $\ddot{\eta}(\tau)$ are the velocity and the acceleration of the free water surface;
- m_∞ is the so-called added mass at infinite frequency, i.e. mass of the oscillating water column plus an additional mass which accounts for the fluid that is displaced outside the collector;
- $k_r(\tau)$ is a term that is connected with the radiation of waves [44] called radiation force kernel;
- ρ_w is the mass density of sea water, g is gravity acceleration; S is the area of the cross-section of water column inside the chamber; the chamber is square with side equal to c, as shown in Fig. 1; the product $\rho_w g S \eta(\tau)$ is the stiffness that is originated by potential energy in static conditions;
- $f_e(\tau)$ is the hydrostatic excitation force on the body due to the dynamic pressure resulting from the incident wave;
- $f(\tau)$ is the PTO force and it can be written as $f = -pS$ where p is the relative air pressure in the chamber.

The radiation force kernel and the added mass at infinite frequency can be computed by boundary element method (BEM), e.g. using commercial software like WAMIT [27]. Additionally, in line with commonly accepted procedures in the wave energy sector, this convolution term is approximated using a state-space description [44]. Thus we introduce

$$\begin{aligned} \dot{\boldsymbol{x}}_{\boldsymbol{r}}(\tau) &= \boldsymbol{A}_{\boldsymbol{r}}\boldsymbol{x}_{\boldsymbol{r}}(\tau) + \boldsymbol{B}_{\boldsymbol{r}}\dot{\eta}(\tau), \\ \int_0^\tau k_r(\tau-\xi)\dot{\eta}(\xi)\mathrm{d}\xi &\approx \boldsymbol{C}_{\boldsymbol{r}}\boldsymbol{x}_{\boldsymbol{r}}(\tau), \end{aligned} \quad (2)$$

where the radiation model's state vector $\boldsymbol{x}_{\boldsymbol{r}} \in \mathbb{R}^r$ is dimensionless thus $\boldsymbol{A}_{\boldsymbol{r}} \in \mathbb{R}^{r\times r}$, $\boldsymbol{B}_{\boldsymbol{r}} \in \mathbb{R}^r$ and $\boldsymbol{C}_{\boldsymbol{r}} \in \mathbb{R}^{1\times r}$ have respectively the dimension of inverse time, inverse length and force.

2.1.1 State space formulation

A state space description of the whole system dynamics is obtained from the previous equations. Define the global physical state of the system, $\boldsymbol{x}_{\boldsymbol{c}}$, and the system input, u_c, as

$$\boldsymbol{x}_{\boldsymbol{c}} = \begin{pmatrix} \dot{\eta} \\ \eta \\ \boldsymbol{x}_{\boldsymbol{r}} \end{pmatrix} \in \mathbb{R}^n, \qquad u_c = f_e + f, \quad (3)$$

where $n = 2 + r$ is the dimension of state space. Then, the associated dynamic equation is

$$\dot{\boldsymbol{x}}_{\boldsymbol{c}}(\tau) = \boldsymbol{A}_{\boldsymbol{c}}\boldsymbol{x}_{\boldsymbol{c}}(\tau) + \boldsymbol{B}_{\boldsymbol{c}}u_c(\tau), \quad (4)$$

where

$$\begin{aligned} \boldsymbol{A}_{\boldsymbol{c}} &= \begin{pmatrix} 0 & \frac{-\rho_w g S}{m_\infty} & \frac{-1}{m_\infty}\boldsymbol{C}_{\boldsymbol{r}} \\ 1 & 0 & \boldsymbol{0}_{\boldsymbol{1}\times\boldsymbol{r}} \\ \boldsymbol{B}_{\boldsymbol{r}} & \boldsymbol{0}_{\boldsymbol{r}\times\boldsymbol{1}} & \boldsymbol{A}_{\boldsymbol{r}} \end{pmatrix} \in \mathbb{R}^{n\times n}, \\ \boldsymbol{B}_{\boldsymbol{c}} &= \begin{pmatrix} 1 \\ 0 \\ \boldsymbol{0}_{\boldsymbol{r}\times\boldsymbol{1}} \end{pmatrix} \in \mathbb{R}^n, \end{aligned} \quad (5)$$

where $\boldsymbol{0}_{\boldsymbol{a}\times\boldsymbol{b}}$ indicates a matrix of zeros $\in \mathbb{R}^{a\times b}$.

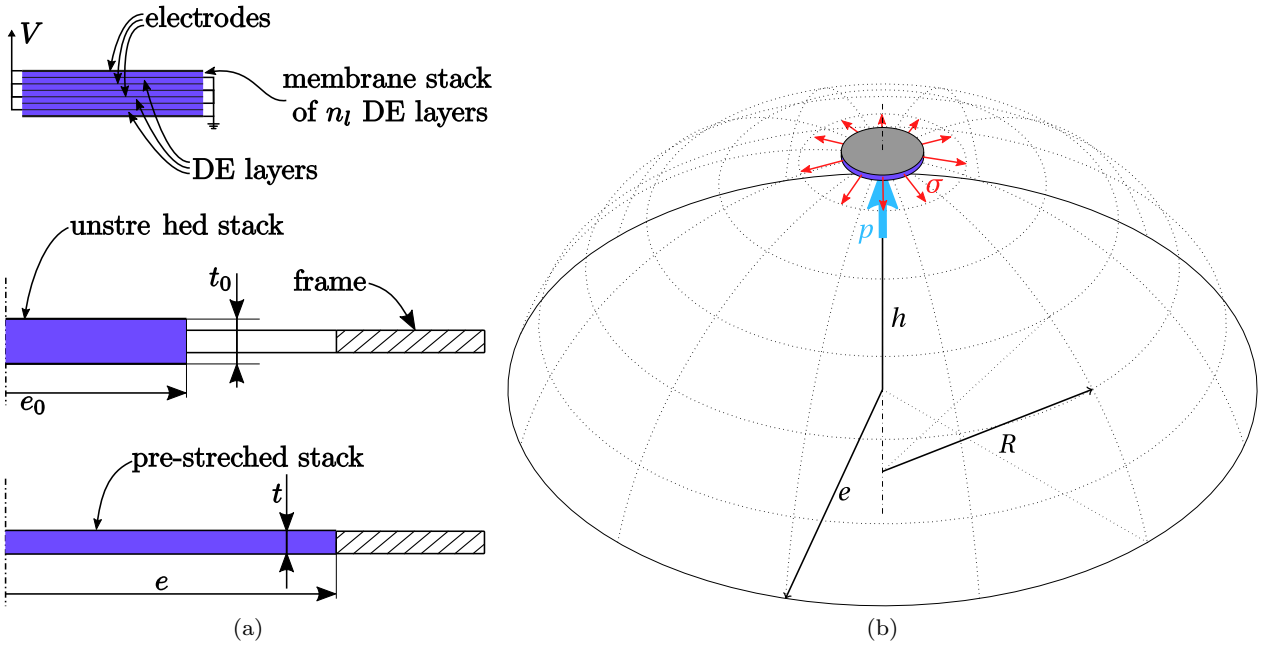

Fig. 2: (a) The multi-layered stacked structure, in which DE layers are alternated with compliant electrodes (top), layout of the CD-DEG (only 1/2 of the geometry is shown) in its unstreched configuration (middle), layout of the CD-DEG in its pre-stretched configuration mounted on a supporting frame (bottom). (b) ICD-DEG deformed shape under the hypothesis of spherical deformation. Figure shows the force balance of the infinitesimal element at the DEG tip.

2.2 ICD-DEG model

The ICD-DEG consists of n_l layers of dielectric elastomer (DE) coated with compliant electrodes, that are piled-up to form a stack. The DE membranes are electrically connected in parallel with alternating polarities of adjacent layers, as shown in Fig. 2a (top). The multi-layered architecture potentially allows compact arrangement of large amounts of material, while guaranteeing homogeneous stretches and electric fields within the layers [43]. The ICD-DEG has thickness t_0 and a radius e_0 in the initial unstretched configuration (see Fig. 2a-middle). The ICD-DEG is equi-biaxially pre-stretched and is clamped along its perimeter at radius e and thickness t. Hence, the value of the pre-stretch is $\lambda_p = e/e_0$ (see Fig. 2a-bottom). The membrane is assumed to be incompressible, therefore $t = t_0/\lambda_p^2$.

When opposing sides of the ICD-DEG are subjected to a differential pressure, p, and to an electric potential difference, V, the ICD-DEG undergoes an out-of-plane axi-symmetric (bubble-like) deformation (area expansion), as shown in Fig. 2b. In the figure, h identifies the resultant displacement of the ICD-DEG tip.

In order to describe the interaction between the OWC system and the ICD-DEG, a single degree of freedom model is chosen, as presented in [30]. The model is based on the following assumptions:

1. The deformed ICD-DEG is a spherical cap with radius R, as showed in Fig. 2b. Owing to this assumption, variable h univocally describes the geometric configuration of the ICD-DEG.
2. The ICD-DEG local deformation is prevalently equibiaxial, therefore the meridian and circumferential stretches (λ_1, λ_2) are equal, namely $\lambda_1 = \lambda_2 = \lambda$.
3. The ICD-DEG capacitance is assumed to be equivalent to that of a planar circular capacitor with variable thickness.
4. The dynamics of the ICD-DEG are negligible with respect to the mass of the water inside the chamber, and the inertial and volume forces of the membrane are negligible with respect to the electro-elastic forces, as further pointed out in the case study in Sect. 4.

The equation describing the ICD-DEG response is the following force balance on the membrane tip element (see Fig. 2b):

$$p\frac{R}{2} = \frac{t_0\sigma}{\lambda^2}, \tag{6}$$

where σ is the local equibiaxial stress. From Eq. (6), we can obtain the value of p as

$$p = \frac{4ht_0\sigma}{\lambda^2\left(h^2+e^2\right)} \tag{7}$$

where λ is the stretch at the ICD-DEG tip:

$$\lambda = \frac{h^2 + e^2}{e e_0} \tag{8}$$

and $\sigma(h, E)$ reads as follows [30]:

$$\sigma = 2k_1 \frac{\lambda^2 - \lambda^{-4}}{I_1 - 2\lambda^2 - \lambda^{-4}} - \epsilon E^2. \tag{9}$$

The fist term in Eq. (9) is a purely elastic stress, calculated using a hyperelastic Gent model [30], featured by the constitutive parameters k_1 and I_1. The second term is an electrostatic stress, in particular ϵ is the dielectric constant of the DE and E is the electric field at the ICD-DEG tip, obtained as follows:

$$E = n_l \frac{\lambda^2 V}{t_0}. \tag{10}$$

The capacitance of the DEG can be obtained as shown in [30] by:

$$C = \frac{Q}{V} = n_l^2 \frac{\pi \epsilon e e_0 \lambda}{3 t_0} \left(\lambda^2 + \frac{e}{e_0}\lambda + \frac{e^2}{e_0^2} \right), \tag{11}$$

where the total charge on the ICD-DEG assembly is hereby denoted by Q.

2.3 Models coupling

The dynamic coupling between the displacement h of the ICD-DEG model and the elevation η of the hydrodynamics model is obtained introducing the thermodynamic model of the air chamber. In particular, assuming an adiabatic transformation of the air, the following relation applies:

$$p = P_{\text{atm}} \left[\left(\frac{Sd}{\Omega} \right)^{\gamma} - 1 \right], \tag{12}$$

where γ is air's heat capacity ratio, S is the cross-section of the water column, d is the height of the chamber over the sea water level (SWL), and P_{atm} is the atmospheric pressure. Additionally, Ω is the volume of the OWC chamber plus the volume subtended by the ICD-DEG, specifically

$$\Omega = \Omega_d + S\,(d - \eta), \tag{13}$$

with

$$\Omega_d = \frac{\pi h}{6} \left(3e^2 + h^2 \right); \tag{14}$$

2.4 ICD-DEG operation and limits

Based on the one-degree-of-freedom kinematics assumption, the ICD-DEG physical state is fully identified by a couple of physical variables, e.g., one describing the DEG kinematics and the other describing its electrical state. In general, any couple of variables among p, f, E, η, h, V, Q can be chosen to characterize the system state. During its operation, the ICD-DEG performs a cyclical sequence of electro-mechanical transformations that can be represented on two-axis diagrams by referring to a couple of independent state variables [25].
In the present application, it is convenient to employ either a $\eta - f$ or a $Q - V$ diagram. The $\eta - f$ plane is of utility in the control optimisation procedure presented in this paper, as it provides direct insight on the PTO force as a function of the WEC displacement. The $Q - V$ plane is useful for practical driving of the electrical variables and DEG control.

In general, the operation of a DEG is subjected to physical and operating constraints [25]. Such constraints depend on the mathematical form of the DEG electro-mechanical response and on physical failure mechanisms that limit the functionality of the DEG as explained in [30], and they can be represented by curves on the $\eta - f$ or $Q - V$ plane, as shown in Fig. 3.
The curves relative to the different constraints identify a closed set of physically admissible states for the DEG, referred to as the *feasible region*.

The mathematical description of the ICD-DEG operating constrains is summarized in the following.

2.4.1 Electrical Breakdown

Electrical breakdown of a DE occurs if the electric field exceeds a limiting value, provoking permanent damage to the dielectric layers. This sets the constraint [38, 41]:

$$E < E_{BD}, \tag{15}$$

where E_{BD} is the electric field at which breakdown occurs. This is a parameter of the elastomer and hereafter is assumed as constant. For the ICD-DEG this constraint is satisfied whenever the inequality Eq. (15) is verified in the center of the membrane (i.e. at the tip of the dofrmed shape), where the thickness is smaller and the electric field is maximum [43].

The limit curve representing electrical breakdown can be represented on a $\eta - f$ plane (see Fig. 3a) upon manipulation of Eqs. (6-14), by replacing $E = E_{BD}$ into Eq. (9). Similarly, the break-down curve can be represented on the $Q - V$ plane (Fig. 3b).

2.4.2 Mechanical Rupture

The simplest criterion for elastomeric materials [16] rupture claims that, to prevent mechanical rupture, the following condition must be satisfied:

$$\lambda < \lambda_u. \tag{16}$$

Here, λ_u is the rupture stretch (measured in a uniaxial rupture test) and it is a constant that depends only on the considered DE material. Inverting Eq. (8), Eq. (16) results in a couple of constrains on the maximum and minimum admissible values of h, that are h_{MAX} for the positive side and h_{MIN} for the negative side (with $h_{\mathrm{MIN}} = -h_{\mathrm{MAX}}$).

The conditions can be drawn on the $\eta - f$ and on the $Q - V$ plane as shown in Figs. 3a and 3b. In particular, on the $Q - V$ plane, the rupture condition is represented by a single iso-capacitance line crossing the axes origin (the ICD-DEG capacitance at $h = h_{\mathrm{MIN}}$ and $h = h_{\mathrm{MAX}}$ is the same).

2.4.3 Electro-Mechanical Buckling

In order to work properly, the DE membrane is required to remain in tension during its functioning. If the total electromechanical stress σ on the ICD-DEG layers falls to zero, the material wrinkles and the transduction mechanism fails. The following condition must thus hold:

$$\sigma > 0. \tag{17}$$

Buckling condition is particularly critical in the configurations in which the deformation, and thus the stress, is minimum, e.g., the flat equilibrium configuration. In practice, buckling is prevented by choosing an appropriate level of pre-stretch and limiting the electric field on the ICD-DEG.
The buckling condition, $\sigma = 0$, corresponds to null air gauge pressure, $p = 0$, i.e., a straight horizontal line on the $\eta - f$ plane. On the $Q - V$ plane the constraint is instead represented by a non-trivial curve obtained by algebraic rearrangement of Eqs. (9-11).

2.4.4 Other constraints

There exist other constraints which bound the ICD-DEG operating spaces on the $\eta - f$ and $Q - V$ planes, not related to the failure mechanisms.

The $\eta - f$ feasible region is further bounded by the purely mechanical response of the DEG, i.e., the curve providing the DEG force at null electric field (see Fig. 3a).
The $Q - V$ feasible region is instead further bounded by the iso-capacitance line corresponding to minimum ICD-DEG capacitance, i.e., the capacitance at $h = 0$ and $\lambda = \lambda_p$ (see Fig. 3b).

2.4.5 Feasible Region

In compliance with previous works on energy harvesting from dynamical systems [20] and on DEGs [26], the above mentioned PTO constraints can be represented on a $\eta - f$ diagram (Fig. 3a) and on a $Q - V$ diagram (Fig. 3b), and they bound a feasible region represented by light blue surfaces.
On the $\eta - f$ plane, the feasible region is non-convex, and it is the union of two sub-regions, one corresponding to upward ICD-DEG expansion ($\eta > 0$) and one to downward ICD-DEG expansion ($\eta < 0$). On the $Q - V$ diagram, instead, a single feasible region exists which symmetrically holds for both upward and downward expansions.

Practical controls of DEGs can be defined by a sequence of operations resulting in a closed loop cycle on the $\eta - f$ and $Q - V$ plots (e.g., blue closed loops in Fig. 3).
In order for a DEG to positively output electrical energy such a cycle should be performed anti-clockwise on both the considered diagrams.

The ideal control cycle that provides maximum energy conversion is bounded by the limiting constraint curves, e.g. $O - D - C - B - A - O$ in Fig. 3, i.e., the DEG is charged to the maximum electric field when the capacitance is maximum, then is kept at the maximum electric field (compatibly with buckling and breakdown), and it is discharged when its capacitance is minimum.

The energy generated by the DEG in a cycle is numerically equal to the area enclosed by the control loop cycle either on the $\eta - f$ or the $Q - V$ plane (namely, the maximum cyclic convertible energy is equal to the area of cycle $O - D - C - B - A - O$). The ratio between the energy generated in a generic control cycle (i.e., the area enclosed by the cycle trajectory) and the maximum convertible energy is hereafter indicated with ζ, and it provides a measure of how close to the limit constraints the DEG is operating.

To achieve $\zeta = 1$, an ideal forcing would be required which makes the DEG stretch-up to its mechanical rupture limit. In Poly-OWC application, instead, the maximum deformation of the DEG results from the complex dynamic interaction with the OWC subsystem, which will also govern the trajectory of the optimal control cycle. That is, in order to maximize the energy converted in a cycle by the Poly-OWC, a proper modulation of the electrical load on the DEG is required to positively influence the overall system dynamics.

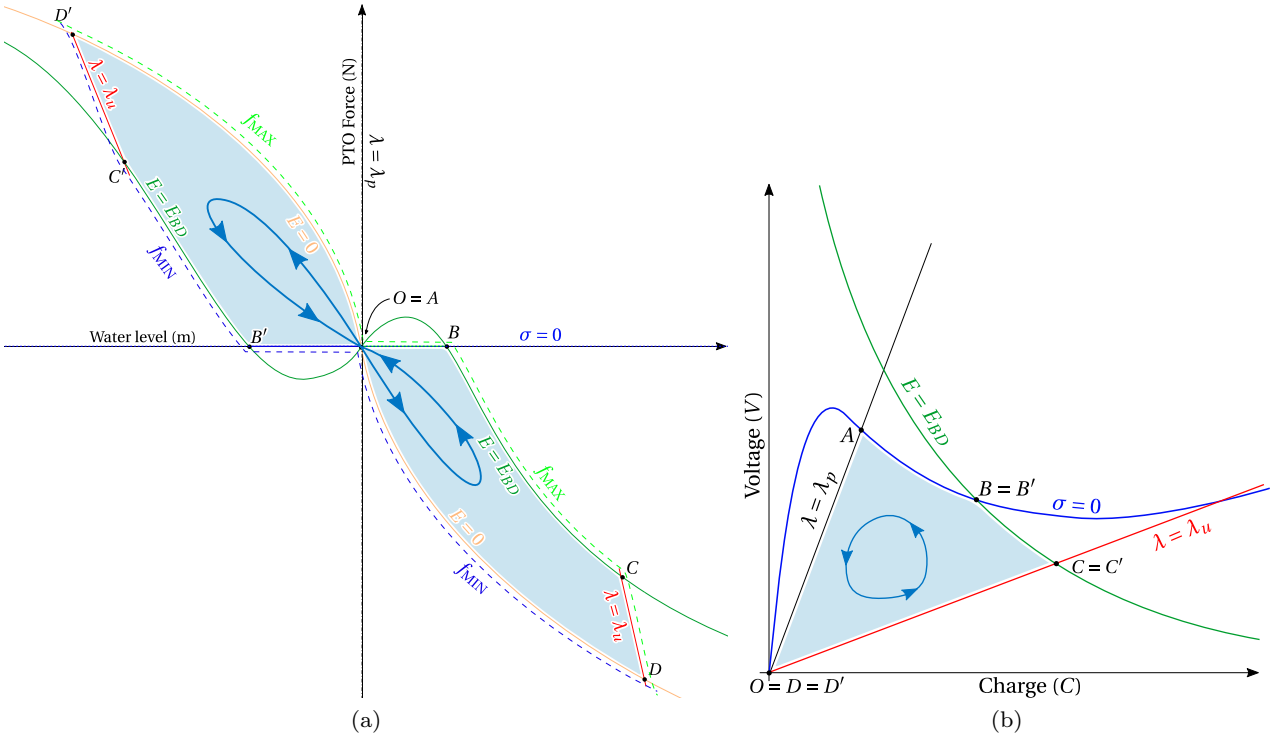

Fig. 3: (a) The $\eta - f$ plane with the ICD-DEG operating constraint curves. The ICD-DEG feasible region is coloured in blue. (b) The $Q - V$ plane with the ICD-DEG operating constraint curves. The ICD-DEG feasible region is coloured in blue.

3 Power Output Optimization

This section deals with the formulation of an optimum control problem, which consists in the maximisation of the Poly-OWC power output based on the system dynamic model.

With this procedure, optimal time-series of the DEG control variables (namely, the electrical control cycles) are determined in order to maximize the power produced by the device in a fixed time horizon while enforcing the satisfaction of the operating constraints discussed before.

3.1 Background and Motivation

The performance of a WEC device depends on its dynamical response and dynamical tuning with the incoming waves. Optimality conditions for wave power conversion were formalised by Falnes [12], who found out that the maximum useful absorbed power for a WEC oscillating in one mode is achieved by the *complex conjugate control*. Indicating by Z_{sys} the mechanical impedance of the WEC system, the optimal load impedance of the PTO has to equal the complex conjugate of the system impedance, Z^*_{sys}.

Such a control maximises the energy absorbed by the PTO machinery, $\mathcal{E}_a$, that is equal to:

$$\mathcal{E}_a = -\int_{-\infty}^{\infty} \dot{\eta}(\tau) f(\tau) \mathrm{d}\tau. \tag{18}$$

In Eq. (18) the PTO machinery is assumed ideal, which implies that the absorbed mechanical energy coincides with the harvested energy.

In practice, the complex-conjugate control results in large WEC oscillation amplitudes and requires a PTO system with four-quadrant force-velocity (or force - displacement) characteristic. In practical applications, restrictions are present both on the maximum allowed displacements of a WEC and on the load characteristic of the PTO (see, for instance, the $\eta - f$ characteristic of an ICD-DEG in Fig. 3a).

The problem of the maximal energy convertible by oscillating systems in the presence of force and displacement constraints has been investigated in literature both with reference to vibration energy harvesting in general [15, 20] and with specific reference to wave energy harvesting [7, 9, 14]. For example, it has been found that the control strategy which guarantees maximum power conversion from a damped oscillating body equipped with a PTO (e.g., a WEC) in the presence of

oscillation amplitude constraints is a *latching-like control*, which consists in keeping the body fixed in the maximum displacement positions during certain intervals of the oscillation cycle [14, 15].

An efficient method to solve a model-based dynamic optimisation problem handling different types of constraints is using a discrete time-domain formulation. The output of the optimisation procedure are control variables' time-series that maximize the objective function over a certain time interval (the prediction horizon), while enforcing the satisfaction of the operating constraints. In a previous paper [29], such a formalism has been used to design a DEG-based PTO for a flap-type WEC based on a set of optimum control trajectories.

A formalism that is commonly applied to WECs control, that uses this procedure, is *model predictive control* (MPC) [7, 14]. In DEG-based WECs, though theoretically attractive, a real-time implementation of the whole optimisation procedure on a wave-by-wave basis is unlikely [17], mainly due to the heavy computational burden. However the solution of the power output optimisation problem can be used to extrapolate control heuristics, thus limiting the effect of inaccuracy in the dynamic model used for the optimisation, while pursuing a closed-loop control implementation.

In the following, we present a time-domain discretisation of the Poly-OWC dynamic model aimed at the solution of the power output optimisation problem in steady-state periodic oscillations.

3.2 Discrete model

In this section, a discretisation of Eqs. (4)-(5) is presented using zero-order-hold with a discretisation time-step, T_s. This method has the advantage to be intrinsically stable [37], it can be applied to multi-input multi-output (MIMO) systems and it allows easy writing of the objective function (see Sect. 3.5). The discretised system obtained from Eq. (4) is:

$$\boldsymbol{x_d}[k+1] = \boldsymbol{A_d}\boldsymbol{x_d}[k] + \boldsymbol{B_d}u_d[k], \tag{19}$$

where

$$\boldsymbol{A_d} = e^{\boldsymbol{A_c}T_s}, \quad \boldsymbol{B_d} = \boldsymbol{A_c}^{-1}\left(e^{\boldsymbol{A_c}T_s} - \boldsymbol{I_n}\right)\boldsymbol{B_c}, \tag{20}$$

and u_d, $\boldsymbol{x_d}$ are obtained by using a zero-order-hold discretization method with sample time T_s:

$$\boldsymbol{x_d}[k] = \boldsymbol{x_c}(kT_s), \quad u_d[k] = u_c(kT_s) \tag{21}$$

where $k \in \mathbb{N}$. In the following, parenthesis (τ) is used for continuous-time variables, and brackets $[k]$ for discrete time.

3.3 Prediction Horizon State Space Evolution

We describe the evolution of the system as a prediction obtained from instant $k = 0$ along a defined horizon of N steps [4]. The evolution of the state can be obtained by the recursion of Eq. (19), using $k = 0, \ldots, N$, and yielding to the following matrix form:

$$\underset{1\to N}{\boldsymbol{x_d}} = \boldsymbol{\Phi}\boldsymbol{x_d}[0] + \boldsymbol{\Gamma}\underset{0\to N-1}{u_d}, \tag{22}$$

where we have introduced a prediction vector notation over N time-steps and it is defined for $\boldsymbol{x_d}$ as follows:

$$\underset{1\to N}{\boldsymbol{x_d}} = \begin{pmatrix} \boldsymbol{x_d}[1] \\ \boldsymbol{x_d}[2] \\ \vdots \\ \boldsymbol{x_d}[N] \end{pmatrix} \in \mathbb{R}^{nN} \quad \text{with } \boldsymbol{x_d} \in \mathbb{R}^n. \tag{23}$$

Equation (23) provides the prediction for $\boldsymbol{x_d}$ in a horizon between 1 and N. In the following pages, the same notation is used for all the variables (scalar and vector). The matrix $\boldsymbol{\Phi} \in \mathbb{R}^{nN\times n}$ in Eq. (22) is a prediction system matrix and $\boldsymbol{\Gamma} \in \mathbb{R}^{nN\times N}$ is the prediction input matrix (also called Toeplitz matrix [34]):

$$\begin{aligned} \boldsymbol{\Phi} &= \begin{pmatrix} \boldsymbol{A_d} \\ \boldsymbol{A_d}^2 \\ \vdots \\ \boldsymbol{A_d}^N \end{pmatrix}, \\ \boldsymbol{\Gamma} &= \begin{pmatrix} \boldsymbol{B_d} & 0 & \cdots & 0 \\ \boldsymbol{A_d}\boldsymbol{B_d} & \boldsymbol{B_d} & \cdots & 0 \\ \vdots & \vdots & \ddots & \vdots \\ \boldsymbol{A_d}^{N-1}\boldsymbol{B_d} & \boldsymbol{A_d}^{N-2}\boldsymbol{B_d} & \cdots & \boldsymbol{B_d} \end{pmatrix}. \end{aligned} \tag{24}$$

If we want to obtain the vectors of inner water level position, $\underset{1\to N}{\eta}$, and velocity, $\underset{1\to N}{\dot{\eta}}$, at any time instant in the prediction horizon from the vector $\underset{1\to N}{\boldsymbol{x_d}}$, we can use these two matrices:

$$\begin{aligned} \boldsymbol{V} &= \begin{pmatrix} 1\,0\,\mathbf{0_{1\times r}}\,0\,0\,\mathbf{0_{1\times r}}\,\cdots\,0\,0\,\mathbf{0_{1\times r}} \\ 0\,0\,\mathbf{0_{1\times r}}\,1\,0\,\mathbf{0_{1\times r}}\,\cdots\,0\,0\,\mathbf{0_{1\times r}} \\ \vdots\,\vdots\;\;\vdots\;\;\vdots\,\vdots\;\;\vdots\;\;\ddots\;\vdots\,\vdots\;\;\vdots \\ 0\,0\,\mathbf{0_{1\times r}}\,0\,0\,\mathbf{0_{1\times r}}\,\cdots\,1\,0\,\mathbf{0_{1\times r}} \end{pmatrix}, \\ \boldsymbol{P} &= \begin{pmatrix} 0\,1\,\mathbf{0_{1\times r}}\,0\,0\,\mathbf{0_{1\times r}}\,\cdots\,0\,0\,\mathbf{0_{1\times r}} \\ 0\,0\,\mathbf{0_{1\times r}}\,0\,1\,\mathbf{0_{1\times r}}\,\cdots\,0\,0\,\mathbf{0_{1\times r}} \\ \vdots\,\vdots\;\;\vdots\;\;\vdots\,\vdots\;\;\vdots\;\;\ddots\;\vdots\,\vdots\;\;\vdots \\ 0\,0\,\mathbf{0_{1\times r}}\,0\,0\,\mathbf{0_{1\times r}}\,\cdots\,0\,1\,\mathbf{0_{1\times r}} \end{pmatrix}, \end{aligned} \tag{25}$$

where $\boldsymbol{V}, \boldsymbol{P} \in \mathbb{R}^{N\times nN}$. In particular:

$$\underset{1\to N}{\dot{\eta}} = \boldsymbol{V}\,\underset{1\to N}{\boldsymbol{x_d}} \quad \text{and} \quad \underset{1\to N}{\eta} = \boldsymbol{P}\,\underset{1\to N}{\boldsymbol{x_d}}. \tag{26}$$

3.4 Terminal state constraint

A particular case that is interesting to analyse is the steady state response to a periodic excitation. This actually well represents the steady state response of the Poly-OWC to monochromatic waves. In this case, we can assume that the optimisation time horizon coincides with the period of the excitation, i.e. period of the monochromatic wave.

The steady state response to a periodic excitation is periodic, thus $\boldsymbol{x_d}[N] = \boldsymbol{x_d}[0]$. Considering Eq. (22) and Eq. (24),

$$\boldsymbol{x_d}[0] = \left(\boldsymbol{I_n} - \boldsymbol{A_d^N}\right)^{-1} \sum_{i=1}^{N} \boldsymbol{A_d^{N-i}} \boldsymbol{B_d} u_d[i-1], \tag{27}$$

where $\boldsymbol{I_a}$ is the identity matrix $\in \mathbb{R}^{a\times a}$. Using the same notation introduced in Eq. (23) we can write Eq. (27) as:

$$\boldsymbol{x_d}[0] = \boldsymbol{\Upsilon} \underset{0\to N-1}{u_d} \tag{28}$$

with $\boldsymbol{\Upsilon} \in \mathbb{R}^{n\times N}$ defined as follows:

$$\boldsymbol{\Upsilon} = \left(\boldsymbol{I_n} - \boldsymbol{A_d^N}\right)^{-1} \left(\boldsymbol{A_d^{N-1}} \boldsymbol{B_d}\ \boldsymbol{A_d^{N-2}} \boldsymbol{B_d} \cdots \boldsymbol{B_d}\right). \tag{29}$$

Using Eq. (28) in Eq. (22), we obtain

$$\underset{1\to N}{\boldsymbol{x_d}} = (\boldsymbol{\Phi\Upsilon} + \boldsymbol{\Gamma}) \underset{0\to N-1}{u_d}, \tag{30}$$

3.5 Objective function

The objective of the optimisation procedure presented here is to compute a control sequence $\underset{0\to N-1}{u_d}$ that maximise an objective function. The objective function, namely the energy absorbed by a DEG-PTO, defined Eq. (18), is calculated within the prediction horizon, coincident with a wave period, T. By setting $T = NT_s$ as the time window prediction horizon, the energy absorbed by the DEG-PTO is obtained by:

$$\mathcal{E}_a = -\int_0^T \dot{\eta}(\tau) f(\tau) \mathrm{d}\tau. \tag{31}$$

In order to apply the optimisation procedure, Eq. (31) becomes:

$$\mathcal{E}_a \approx -T_s \sum_{k=0}^{N-1} \dot{\eta}[k] f[k]. \tag{32}$$

Then, the corresponding discrete-time optimisation problem is

$$\min \left(T_s \sum_{k=0}^{N-1} \dot{\eta}[k] f[k] \right). \tag{33}$$

The index k runs from 0 to $N-1$ because we have chosen the zero-order-hold discretisation method. Rewriting the problem with the notation defined in Eq. (23), Eq. (33) becomes:

$$\min \left(T_s \underset{0\to N-1}{\dot{\eta}^T} \underset{0\to N-1}{f} \right). \tag{34}$$

This optimisation problem presents two different unknown variables: $\dot{\eta}$ and f. We therefore need to express the velocity of the water level as a function of the PTO force using the system discretised dynamic equation, Eq. (30).

However, the indexes of the state vector $\underset{1\to N}{\boldsymbol{x_d}}$ (and, thus, of the velocity) in Eq. (30) do not match with the indexes present in Eq. (34). Indeed, in the former equation, indexes run from 1 to N and not from 0 to $N-1$. Thus, the velocity vector needs to be modified accordingly. To do this, we can use the initial state, $\boldsymbol{x_d}[0]$. The result is:

$$\underset{0\to N-1}{\boldsymbol{x_d}} = \boldsymbol{X}\boldsymbol{x_d}[0] + \boldsymbol{Z} \underset{1\to N}{\boldsymbol{x_d}} \tag{35}$$

using the following matrices

$$\begin{aligned} \boldsymbol{X} &= \begin{pmatrix} \boldsymbol{I_n} \\ \boldsymbol{0_{n(N-1)\times n}} \end{pmatrix}, \\ \boldsymbol{Z} &= \begin{pmatrix} \boldsymbol{0_{n\times n(N-1)}} & \boldsymbol{0_{n\times n}} \\ \boldsymbol{I_{n(N-1)}} & \boldsymbol{0_{n(N-1)\times n}} \end{pmatrix}, \end{aligned} \tag{36}$$

where $\boldsymbol{X} \in \mathbb{R}^{nN\times n}$, $\boldsymbol{Z} \in \mathbb{R}^{nN\times nN}$. Using Eq. (30) and Eq. (28) in Eq. (35), we can write:

$$\underset{0\to N-1}{\boldsymbol{x_d}} = \boldsymbol{X\Upsilon} \underset{0\to N-1}{u_d} + \boldsymbol{Z}\left(\boldsymbol{\Phi\Upsilon} + \boldsymbol{\Gamma}\right) \underset{0\to N-1}{u_d}. \tag{37}$$

For the sake of clarity, we define the matrices that correlate the vectors of velocity and position (at the various time instants) to the input vector, $\underset{0\to N-1}{u_d}$, as:

$$\boldsymbol{\Omega_V} = \boldsymbol{V}\left(\boldsymbol{X\Upsilon} + \boldsymbol{Z}\left(\boldsymbol{\Phi\Upsilon} + \boldsymbol{\Gamma}\right)\right), \tag{38}$$

$$\boldsymbol{\Omega_P} = \boldsymbol{P}\left(\boldsymbol{X\Upsilon} + \boldsymbol{Z}\left(\boldsymbol{\Phi\Upsilon} + \boldsymbol{\Gamma}\right)\right), \tag{39}$$

where $\boldsymbol{\Omega_V} \in \mathbb{R}^{N\times N}$, $\boldsymbol{\Omega_P} \in \mathbb{R}^{N\times N}$. As a matter of simplification, in the following pages, the underlined variable refers to the prediction of a generic variable in a horizon between 0 and $N-1$ as shown here for $\boldsymbol{x_d}$:

$$\underset{0\to N-1}{\boldsymbol{x_d}} = \underline{\boldsymbol{x_d}}. \tag{40}$$

Using the same notation, we can obtain the velocity and the position from step 0 to step $N-1$ as:

$$\underline{\dot{\eta}} = \boldsymbol{\Omega_V}\underline{u_d}, \qquad \underline{\eta} = \boldsymbol{\Omega_P}\underline{u_d}. \tag{41}$$

Finally, the objective function in Eq. (34) can be rewritten as:

$$\min_{\underline{f}} \left(T_s \left(\underline{f}^T \boldsymbol{\Omega_V} \underline{f} + \underline{f_e}^T \boldsymbol{\Omega_V} \underline{f} \right) \right) \tag{42}$$

which is a quadratic problem in $\underline{f}$, written in a convenient form for computational solution.

3.6 Discrete time constraints

This section explains how to discretise the constraints introduced in Sec. 2.4 to include them in the optimisation problem. Moreover, to prevent the optimal controller from charging/discharging the DEG excessively fast (which is not implementable with practical power conditioning electronics), a further constrain is added on the maximum current delivered by the electronic harvesting circuit.

3.6.1 Feasible Region

The feasible region for an ICD-DEG has been introduced in Sec. 2.4.5. As the optimisation problem (42) is formulated in terms of the PTO force, f, the $\eta - f$ representation of the feasible region is hereafter employed.

Considering Fig. 3a, we can reduce the constraints to two main non-linear constraints on f as:

$$f_{\text{MIN}} < f < f_{\text{MAX}}, \tag{43}$$

where f_{MAX} and f_{MIN} represent the upper and lower envelopes of the curves bounding the feasible region, as shown in Fig. 3a.

It is required that the state of the PTO (identified by f and η) is included within the feasible region at any time instant. This condition reads as follows:

$$\mathbf{1_{N\times 1}} f_{\text{MIN}} < \underline{f} < \mathbf{1_{N\times 1}} f_{\text{MAX}} \tag{44}$$

where $\mathbf{1_{a\times b}}$ is a constant matrix of ones $\in \mathbb{R}^{a\times b}$. It is worth noticing that, as the feasible region is non-convex, it cannot be approximated by a linear convex set, thus the combination of objective function (42) and constraints (44) does not provide a quadratic programming problem.

3.6.2 Maximum Current

This constraint is prescribed by considering that the control electronics of the system cannot generate an infinite current to charge the DEG electrodes. For this reason, we have set a maximum value, I_{MAX}, for the modulus of the current that can be delivered to the DEG-PTO.

Using the value of $\underline{f}$ and $\underline{\eta}$ we can obtain the value of the electric field. The electric field is fed into Eq. (10) to obtain the value of the voltage on the DEG. The capacitance $\underline{C}$ of the ICD-DEG is obtained from Eq. (11). Using $\underline{V}$ and $\underline{C}$ we can obtain the value of the DEG charge as:

$$\underline{Q} = \underline{C} \circ \underline{V}, \tag{45}$$

where "$\circ$" identifies the Hadamard product [19], i.e., an entry-wise multiplication. The current is equal to the time rate of charge variation. For the periodic case, this relation can be written in a linear form as:

$$\underline{I} = \frac{1}{T_s} \begin{pmatrix} 1 & 0 & 0 \cdots & 0 & -1 \\ -1 & 1 & 0 \cdots & 0 & 0 \\ 0 & -1 & 1 \cdots & 0 & 0 \\ \vdots & \vdots & \vdots \ddots & \vdots & \vdots \\ 0 & 0 & 0 \cdots & -1 & 1 \end{pmatrix} \underline{Q}. \tag{46}$$

Finally, the constraint can be written as:

$$\underline{I} < \mathbf{1_{N\times 1}} I_{\text{MAX}}. \tag{47}$$

4 Numerical simulation

In this section, the optimisation procedure described in Sec. 3 is applied to a numerical case study. Based on the results, real-time control heuristics are deduced and their effectiveness is assessed in panchromatic waves. The deduced real-time control is based on the direct measurement of some physical variables and the long-term prediction/estimate of statistical parameters of the incoming waves (e.g. significant wave height, peak period, etc.).

4.1 Case study data

In this section, we report the parameters of the Poly-OWC [36] and the characteristics of the incoming waves used to perform the power output optimisation and the consequent control validation in panchromatic waves.

The dimensions of the reference OWC chamber are based on the Pico Plant off the coasts of Azores, Portugal [11], and the hydrodynamic parameters, obtained

using WAMIT. The state space representation of radiation force is performed using 4 additional states.

The dimensions of the Poly-OWC and the characteristics of the membrane are shown in Tab. 1. In particular, the considered DE material [42] is a soft silicone that presents suitable characteristics for energy harvesting operations, like low mechanical stiffness and large dielectric constant. This material is not yet a commercial product but it is taken as representative of an optimised DE material specifically produced for DEG application.

It has been verified that, with the considered dimensions, the ICD-DEG dynamics are negligible compared to that of the water column, as postulated in Sect. 2.2. Indeed, approximating the set of the OWC and the ICD-DEG as a two-body dynamical system (including the DEG inertia) [42], it has been estimated that the natural frequency of the ICD-DEG free oscillations (in the presence of fixed water column level) is one order of magnitude higher than the natural frequency of the OWC oscillations (in the presence of in-phase ICD-DEG deformations).

Parameters	Poly Pico Plant
Width of the chamber, c	$12\,\mathrm{m}$
Chamber cross section area, S	$144\,\mathrm{m}^2$
Height of the air chamber, d	$7.29\,\mathrm{m}$
Water depth within the chamber, b	$8\,\mathrm{m}$
Underwater opening breadth, a	$6\,\mathrm{m}$
ICD-DEG radius, e	$5\,\mathrm{m}$
Pre-stretch, λ_p	3
Initial thickness, t_0	$1.35\,\mathrm{m}$
Electrical breakdown field, E_{BD}	$150\,\mathrm{MV\,m^{-1}}$
Dielectric constant, ϵ	$44.5 \times 10^{-12}\,\mathrm{F\,m^{-1}}$
Rupture stretch, λ_u	7.3
Material parameter, I_1	197.5 [42]
Material parameter, k_1	2.95 MPa [42]

Table 1: Poly-OWC parameters for the reference real-scale device based on the dimensions of the Pico plant.

The excitation force used in the periodic analysis is that of a mono-harmonic incident wave of period $T = 2\pi/\omega$ and wave height H, and is equal to:

$$f_e(\tau) = \frac{H}{2} \cdot \hat{\Gamma}(\omega) \cdot \sin(\omega\tau), \tag{48}$$

where $\hat{\Gamma}(\omega)$ is a frequency-dependent wave excitation coefficient, obtained by BEM analysis.

In the real-time analysis, under the hypothesis of a multi-harmonic incident wave [18] (panchromatic wave) the excitation force can be approximated as a finite sum of monochromatic terms, as:

$$f_e(\tau) = \sum_j \hat{\Gamma}(\omega_j) A_j \sin(\omega_j \tau + \phi_j), \tag{49}$$

where:

- ω_j are the frequencies chosen for the sampling of the spectrum.
- A_j are the amplitudes of the different monochromatic waves, related to the wave spectrum $S_\omega(\omega_j)$ as follows:

$$A_j = \sqrt{2\Delta\omega S_\omega(\omega_j)}. \tag{50}$$

  with $\Delta\omega$ being the step between two consecutive frequency values.
- ϕ_j are random phases between 0 and 2π.

The expression of the spectrum S_ω depends on the frequency ω and a couple of statistical wave parameters. We assume a Bretschneider spectral distribution [5]. Using the significant wave height, H_s and the energy period T_e, S_ω takes the following expressions:

$$S_\omega(\omega) = 262.9 H_s^2 T_e^{-4} \omega^{-5} \exp(-1054 T_e^{-4} \omega^{-4}). \tag{51}$$

The Bretschneider spectrum leads to irregular wave profiles with a relatively large harmonic content, as it features a lower peakedness than most practical spectra obtained from ocean wave data (e.g., JONSWAP spectra) [5]. This is a conservative assumption, which allows the validation of the proposed control heuristics in operating conditions which are significantly different from the monochromatic case.

4.2 Power Output Optimization Results

In this section, we report results relative to the monochromatic wave optimisation procedure described in Sec. 3 in two different cases: without the constraint on the maximum electric current that the power electronics can deliver to the DEG and with such a constraint.

The dynamics optimisation is performed in a wide range of wave amplitudes and periods although in the following only a few relevant cases are shown.

4.2.1 Implementation

The optimal control analysis was performed using MATLAB® scripts and the Opti toolbox [2]. The optimisation procedure was performed using interior point optimiser (IPOPT) [1]. IPOPT implements a primal-dual interior point method [28] and uses line searches based on Filter methods (Fletcher and Leyffer [13]). The optimisation procedure was performed with 200 time-steps ($N = 200$).

4.2.2 Unconstrained Maximum Current

This sub-section reports the simulation results obtained by the optimisation procedure in the case without constraint on the maximum current.

Figures 4 (top left and right) show the tip elevation, the electric field, and the position of the inner water level for two different sea states. The top right plot refers to a sea state with large wave amplitude, thus non linearities are significant. This produces a water level displacement that is far different from a sinusoid. In the top left plot, in contrast, the incoming wave is smaller, therefore the effect of the non-linearities of the system is less influential and it results in a sinusoidal motion of the water level displacement. The membrane activation behaviour shows that the membrane is only active with maximum feasible electric field during part of the cycle, while for the remaining time the membrane is kept inactive. The time history of the electric field can be summarized through the following main phases:

1. Expansion phase: The electric field is kept equal to zero during certain time intervals, at the end of which it instantaneously rises to its highest value.
2. Charging phase: Membrane charging approximately takes place when the membrane deformation is maximum, although the exact charging instants depend on the frequency of the incoming waves, as explained later.
3. Harvesting phase: After charging, the electric field is kept maximum with respect to the physical constraints: the break-down field ($E_{BD} = 150\,\mathrm{MV\,m^{-1}}$) and the buckling condition ($\sigma \geq 0$).
4. Discharging phase: When the tip of the ICD-DEG (or, equivalently, the pressure) crosses zero, the value of the electric field instantaneously goes to zero.

Figures 4 (centre left and right) show the pressure inside the OWC chamber and its derivative for the same sea states. In these figures, the pressure experiences a series of sudden drops in correspondence of the charging instants. Correspondingly, the membrane tip position undergoes a jump. Indeed the instantaneous rise of the electric field in the DE layers is responsible for DEG stress reduction (see Eq. (9)) and for a consequent jump in tip and pressure time series. The pressure is equal to zero during part of harvesting phases, when the DEG is in a state of marginal stability with respect to the loss-of-tension condition ($\sigma = 0$, $p = 0$) due to the applied electric field.

Figures 4 (bottom left and right) show the cumulated electrical energy, $\mathcal{E}_e(\tau)$, supplied by the DEG. This energy is the sum of positive electrical energy fluxes provided in output by the DEG and negative ones received by the DEG in input. The variation of $\mathcal{E}_e$ over a period is equal to the absorbed energy $\mathcal{E}_a$ defined in Eq. (31). $\mathcal{E}_e$ is constant during the expansion phases as the DEG electric field is null. Then, $\mathcal{E}_e$ instantaneously decreases in correspondence of the charging phases, during which electrical energy is spent to charge the DEG. During the harvesting phases the DEG produces a positive electrical energy output as a result of decrease in its capacitance. Finally, at the discharging instant the electrical energy stored in the DEG is recovered and $\mathcal{E}_e$ rapidly increases. Notice that the amount of net electrical energy generated in a cycle compared to the energy spent to charge the DEG increases when the deformation increases.

The same simulations were performed in a variety of sea states beyond those reported in Fig. 4. The same four-phase control behaviour described above has been observed in all the considered sea states.
Based on the different simulations, the starting instant of the charging phase results correlated to the frequency of the incoming waves, and it can be either anticipated or delayed with respect to the instant of maximum deformation of the membrane. In particular, for wave periods shorter than 8.5 s, the charging phase is slightly delayed with respect to the instant in which the distance of the water column free surface from equilibrium becomes maximum, i.e. short after the zero crossing of the air pressure derivative (see right plots in Figures 4). Conversely, for wave periods larger than 8.5 s, the charging phase is slightly anticipated with respect to the instant when the distance of the water column free surface from equilibrium reaches a maximum, i.e. before the zero crossing of pressure derivative (see left plots in Figures 4). Wave period $T = 8.5\,\mathrm{s}$ represents the natural frequency of the system.

The obtained behaviour has the following explanation. Application of the electric field causes a reduction of the ICD-DEG mechanical stiffness. The shorter the time during which the DEG is activated, the stiffer the DEG. When the incoming wave has a period below the resonance period, it is kept activated for a shorter time, so that its natural period approaches the wave period. Instead, when the incoming wave period surpasses the system resonance period, the membrane is kept activated for a longer time in the cycle, its rigidity decreases and its natural period increases. In both cases, the control attempts to tune the system to the incoming wave period. When the height of the incoming waves increases, the need for tuning decreases, because the membrane displacement is already rather large and its performance is weakly affected by dynamical tuning.

As regards charging and discharging behaviour, the modulus of the current on the ICD-DEG is much higher

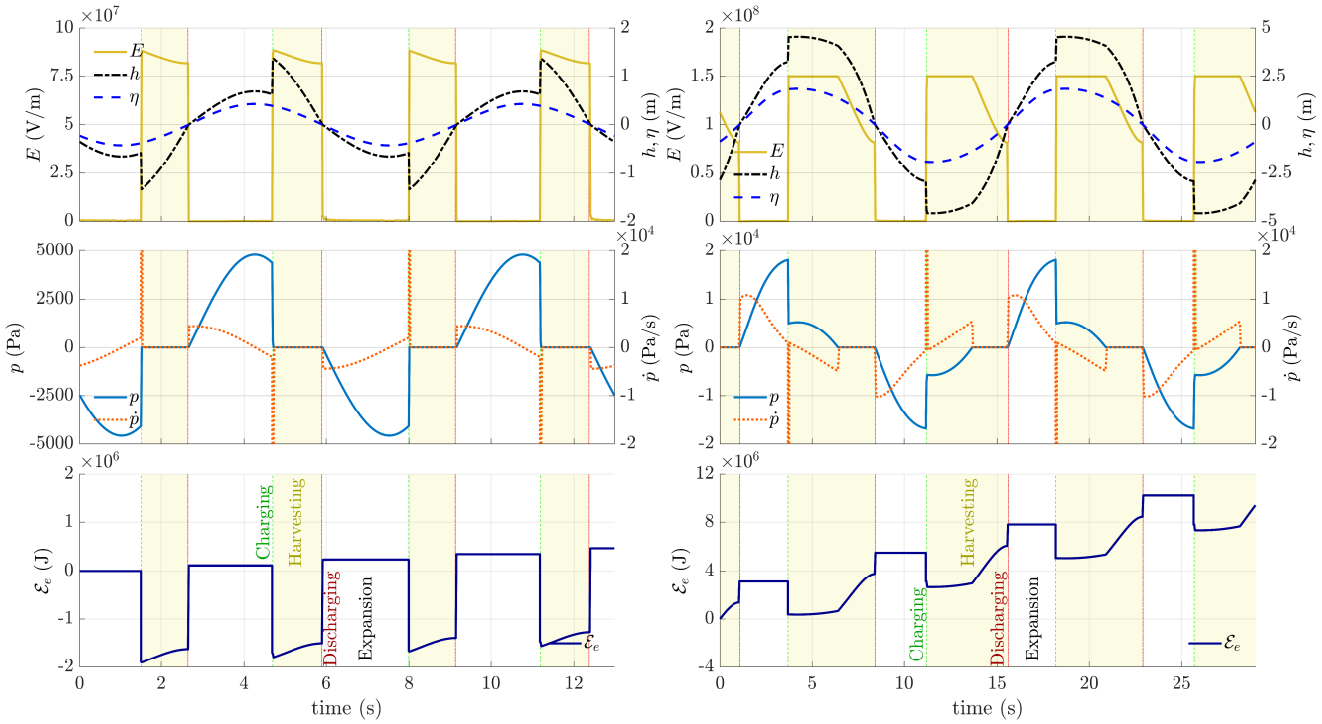

Fig. 4: Optimal electric field E, membrane tip elevation h and water column level η (top plots); optimal pressure inside the chamber p and pressure derivative $\dot{p}$ (central plots); cumulated electrical energy output provided by the DEG (bottom plots). Plots refer to two different sea states: $H = 1\,\mathrm{m}$, $T = 6.5\,\mathrm{s}$ (left), $H = 3\,\mathrm{m}$, $T = 14.5\,\mathrm{s}$ (right).

compared to the harvesting phase. In fact, the ideal controller prescribes DEG charging in one time step. Because the charging is instantaneous, the current is impulsive and its maximum value (in numerical simulations) is equal to Q/T_s. Since this charging mode is not feasible in practice (it would indeed require electronics with extremely high rated power, thus involving very large electrical lossess), in 4.2.3 the behaviour of the same four phase controller is investigated when a constraint on the maximum current is included.

4.2.3 Constrained Current

In this section, the results of the optimisation procedure in the presence of a constraint on the DEG current are compared with previous results without such a constraint. Specifically, here, the current is limited to $I_{\mathrm{MAX}} = 200\,\mathrm{A}$.

Figure 5 (first) shows the optimal solutions for the tip elevation and the water column level. In the figure, the dashed grey line and solid blue line represent the previous result (only for the sea condition with $H = 3\,\mathrm{m}$, $T = 14.5\,\mathrm{s}$), while the dash-dot black line and the dotted line represent the new result with current limitation. Though approximately overlapped to the previous solution, these new results feature better physical consistence, and during charging the membrane tip elevation rises gradually from one equilibrium position (in the absence of the electric field) to another equilibrium position (at maximum electric field). With respect to the previous analysis, the beginning of the charging phase (when the electric field rises from zero to E_{BD}) is anticipated to compensate the non-instantaneous charging time. The water level time series are not significantly different considering the two different DEG charging dynamics.

Figure 5 (second) illustrates the optimal solutions for the electric field and current. As without the electric current limit, the module of the current during ICD-DEG charging and discharging is much larger than during the rest of the cycle, and it keeps to the maximum allowed value for the entire charging/discharging phase.

Figure 5 (third) gives an example of optimal solutions for the relative pressure and pressure derivative. Based on those signals, it is possible to define thresholds for DEG charging/discharging, in order to define a synthetic control procedure that matches the results of optimum control, as further explained in Sec. 4.3.

Figure 5 (fourth) shows the cumulated electrical energy output. Compared to the previously case without current constraint, the energy fluxes relative to charg-

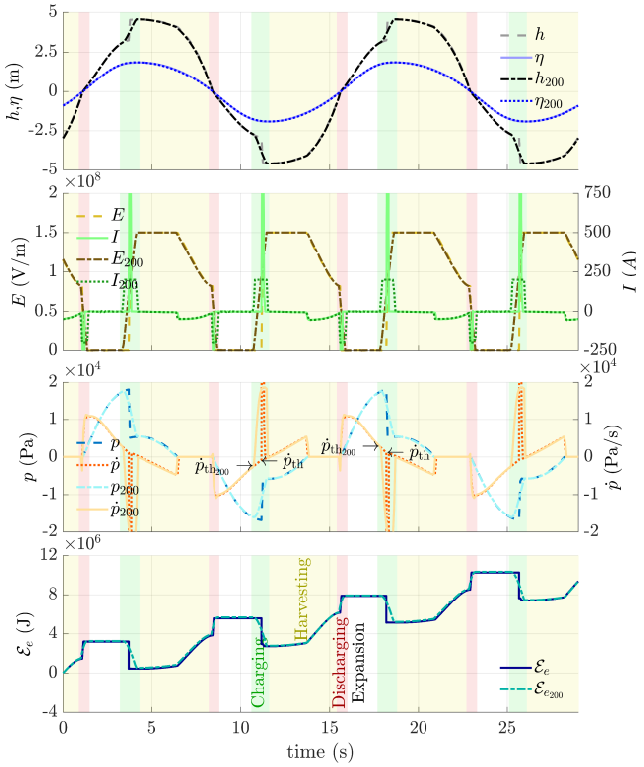

Fig. 5: Comparison between the results without maximum current constraint and the results with maximum current constraint ($I_{\mathrm{MAX}} = 200$ A) for the sea state with $H = 3\,\mathrm{m}$, $T = 14.5\,\mathrm{s}$. Optimal membrane tip elevation h, h_{200} and water column level η, η_{200} (first plot); optimal electric field E, E_{200} and electric current towards the DEG I, I_{200} (second plot); optimal pressure inside the chamber p, p_{200} and pressure derivative $\dot{p}$, p_{200} (third plot); cumulated electrical energy output provided by the DEG (fourth plot).

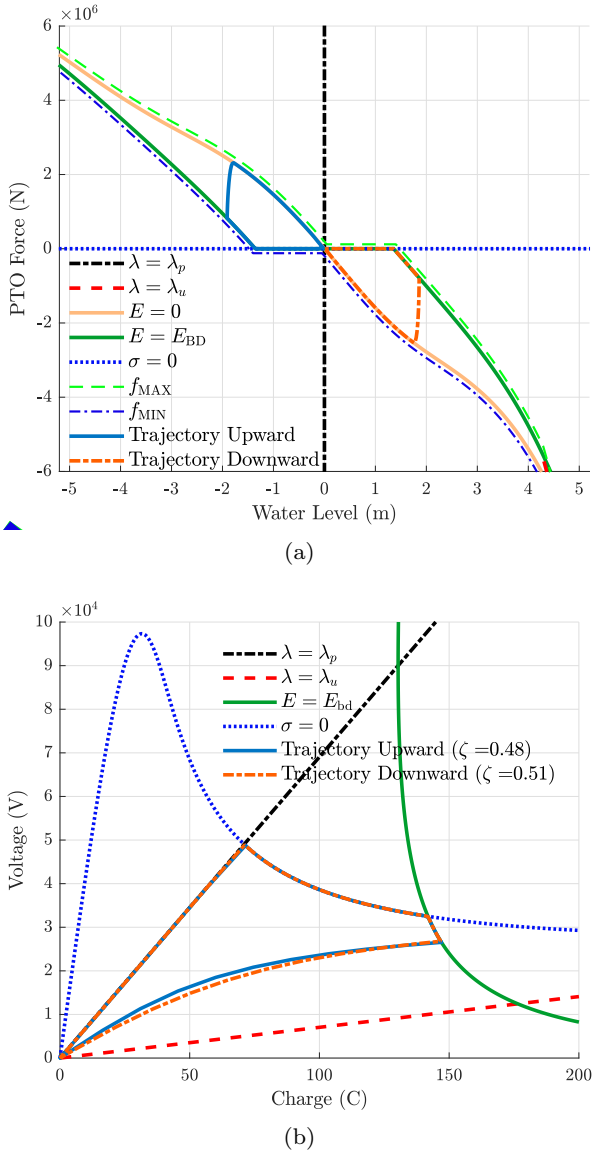

Fig. 6: (a) Feasible region on $\eta - f$ plane (bounded by dash-dot blue and dashed green lines); (b) feasible region on the $Q - V$ plane (dashed red, dash-dot black, dotted blue and solid green lines). The optimal control trajectories (relative to upward and downward DEG expansion) for the case with constrained maximum current are represented by cyan and orange lines.

ing and discharging phase are spread over a finite time interval. Despite the further constraint set by current limitation, the amount of energy harvested in a cycle is practically equal to the case with unconstrained current.

In Fig. 6a, the DEG feasible region and the optimal control trajectories for the considered sea state ($H = 3\,\mathrm{m}$ and $T = 14.5\,\mathrm{s}$) are represented on a $\eta - f$ plane. The dash-dot blue line and the dashed green line indicate the constraint of f_{MIN} and f_{MAX}, respectively (see Eq. (44)). The solid cyan line and the orange dash-dot line represent the trajectories of the PTO force in a period, for upward ($h > 0$) and downward ($h < 0$) DEG deformation respectively. As expected, these trajectories are inside the feasible region. In the figure, the DEG charging phase results in a jump in the $\eta - f$ trajectory from the dash-dot blue line to the dashed green line when the water level is positive, and from the dashed green line to the dash-dot blue line when the water level is negative. The portion of the trajectory where the PTO force is equal to zero identifies the condition $\sigma = 0$.

Figure 6b illustrates the feasible region and the optimal trajectories on a charge-voltage $Q - V$ plane.

In analogy with the $\eta - f$ representation, the optimal trajectories are represented by a cyan solid line and

an orange dash-dotted line respectively. In Fig. 6b, the charging trajectories run on the breakdown curve. The optimal trajectories then move on the breakdown curve until they reach the buckling curve. When the capacitance is minimum, the membrane is discharged and the trajectory on the $Q-V$ plane follows the dash-dot black line, reaching the origin of the axes. The slight difference in the trajectories relative to upward and downward DEG expansion owes to the non-symmetrical behaviour of the system introduced by the non-linear air chamber compressibility model.
For the cycles under investigation, Fig. 6b also reports the values of parameter ζ, i.e., the ratio of the actual energy converted in a cycle and the maximum cyclic convertible energy for the DEG. Although the DEG operates at the maximum electric field (compatible with buckling and breakdown constraint), ζ is approximately equal to 50%, because, as a result of the dynamical interaction with the OWC, its maximum deformation is below the upper bound set by the mechanical rupture condition.

4.3 Real-Time Controller Implementation

In this section the real-time controller is presented and it is applied to a panchromatic case study. The section shows, in order: the logic of the controller; the identification of a control parameter (a pressure derivative threshold) to command the DEG charging and its optimisation through an iterative procedure throughout the different sea states; the comparison of the power output performance with respect to that obtained with a simple controller already presented in a previous work.

4.3.1 Control heuristic synthesis

As explained before, a real-time implementation of the described optimisation procedure in panchromatic waves would be interesting to achieve.

However, the presence of non-linear constraints and the need of a long prediction horizon increases the solution time by several orders of magnitude, making the application of an online optimisation procedure impractical. Nevertheless, the proposed optimisation procedure still provides control logics that can be extrapolated to the irregular waves case.

In effect, a synthetic real-time control can be explicitly deduced from Sec. 4.2.2 and it can be tested in the case of panchromatic waves, using the air pressure signal as the control variable. Indeed, the air pressure can be easily and reliably measured through cheap sensors, and the robustness of pressure reading for Poly-OWC control has been already proven experimentally [40].

With reference to the results presented in Sec. 4.2.2 and 4.2.3, the charging instants can be put in relation with the values of the pressure and of its derivative. The values of the pressure derivative at the DEG charging instants can be used to command the switching of the controller between the expansion phase to the charging phase, while the pressure can be used to switch between the harvesting and the discharging phase.
In particular, the real-time control defined in the following is parametrized using a pressure derivative threshold, $\dot{p}_{\mathrm{th}}$. We define the pressure derivative threshold in a way that it has positive sign if charging occurs after pressure derivative zero-crossing, and negative otherwise.

Using such a threshold we can define the control cycle as follows:

1. Expansion phase: while the capacitance increases, the ICD-DEG is kept inactive. At the beginning of this phase an auxiliary variable $\delta = \mathrm{sign}(\dot{p})$ is defined. Such a variable is used in the following phase to detect whether the ICD-DEG is moving upwards (positive value) or downwards (negative value).
2. Charging phase: the ICD-DEG is electrically activated when the following inequality is satisfied:

$$\delta \dot{p} < -\dot{p}_{\mathrm{th}}, \tag{52}$$

   The current is kept equal to I_{MAX} until the maximum admissible electric field is reached.
3. Harvesting phase: the electric field E is kept equal to E_{MAX}, where E_{MAX} can be equal to E_{BD} or to the electric field necessary to keep the membrane close to the buckling condition. This phase lasts until p crosses zero.
4. Discharging phase: as the relative air pressure crosses zero (i.e., its capacitance is minimum), the DEG is discharged, I is set to $-I_{\mathrm{MAX}}$. I is kept equal to $-I_{\mathrm{MAX}}$ until the ICD-DEG is fully discharged.

We assume that all the hyperelastic and electric parameters of the membrane are known, i.e., complete knowledge of the membrane state at each instant is available, so that it is possible to track the buckling and breakdown conditions during the harvesting phase.

Figure 7 shows the control schematic. In the figure, the "Controller" block implements the control logic explained before. It uses the pressure signal and its derivative in order to follow the DEG-PTO optimal harvesting cycle, taking as charging threshold an optimised $\dot{p}_{\mathrm{th}}$ value received from the "Lookup table" block. This latter is defined as a function that receives the significant wave parameters (H_s and T_e) from an external estimator, e.g. a wave monitoring system, and returns an appropriate value of $\dot{p}_{\mathrm{th}}$. The values of $\dot{p}_{\mathrm{th}}$ are mapped

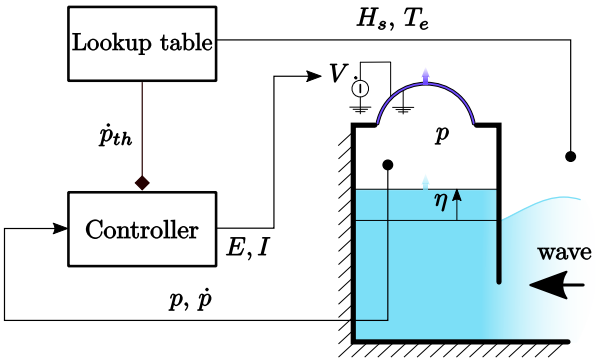

Fig. 7: Schematic of the real-time controller for panchromatic waves.

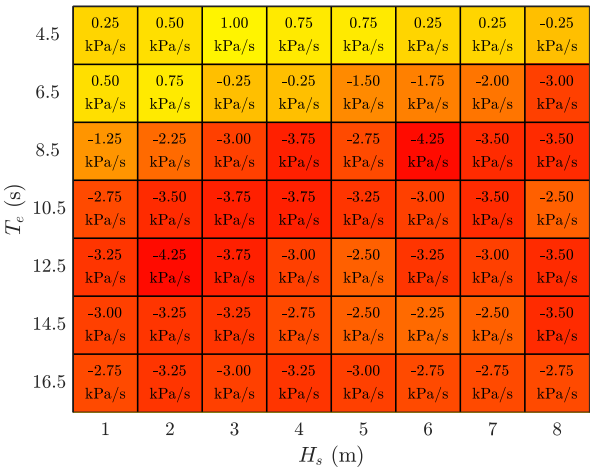

Fig. 8: Derivative pressure threshold, $\dot{p}_{\text{th}}$, to control the DEG charging.

through a model-based optimisation throughout different sea states, as described in the following section. The wave parameters fed into the lookup table are updated on a medium term basis (for example a few tens of minutes) with no need for wave-by-wave prediction.

Interestingly, the control logic deduced form the optimisation procedure is relatively similar to the heuristic control employed in early works on Poly-OWC [30, 36]. That simplified control also has four phases, articulated as follows: 1) the ICD-DEG is kept electrically inactive as its capacitance (or deformation) increases; 2) it is then instantaneously charged when the capacitance reaches maximum value (maximum upward/downward deformation); 3) the electric field is then kept at the maximum value compatibly with break-down and buckling; 4) finally, the ICD-DEG is fully discharged as its capacitance becomes minimum (i.e., in the flat configuration).

In practice, the simplified Poly-OWC control used in [30] and [36] is a particular case of that described above, featuring derivative pressure threshold $\dot{p}_{\text{th}} = 0$. A comparison of the new optimised control with the early controller is provided in the following section.

4.3.2 Optimization of the pressure derivative threshold

The optimal values of the pressure derivative threshold are identified through an iterative procedure performed in MATLAB® Simulink for a set of sea conditions.

For each sea state, several simulations are performed, each with a different value of $\dot{p}_{\text{th}}$ within a defined range.
Specifically, each simulation uses: the model and parameters employed in the power output optimisation procedure with maximum admissible current of 200 A and with panchromatic wave excitation force (see Eq. (49)), the control logic explained before, and a specific value of $\dot{p}_{\text{th}}$. The output of the simulations is the mean power output generated.
At the end of this procedure, for each sea state we can determine the best value of the pressure derivative threshold $\dot{p}_{\text{th}}$ that produces the maximum power output.

The range of the values of significant wave heights and energy periods are:

$$\begin{aligned} T_e &= \big(4.5\,\text{s}, 6.5\,\text{s}, 8.5\,\text{s}, 10.5\,\text{s}, 12.5\,\text{s}, 14.5\,\text{s}, 16.5\,\text{s}\big), \\ H_s &= \big(1\,\text{m}, 2\,\text{m}, 3\,\text{m}, 4\,\text{m}, 5\,\text{m}, 6\,\text{m}, 7\,\text{m}, 8\,\text{m}\big), \end{aligned} \tag{53}$$

As known from literature [8, 17], in order for the wave parameters (H_s and T_e) to be statistically significant (i.e., representative of a panchromatic sea state), they should be calculated over a time span in the order of 30 minutes. Consistently, the simulation used to optimise the value of $\dot{p}_{\text{th}}$ are conservatively run for a time span of 400 times T_e.

The optimal values of $\dot{p}_{\text{th}}$ are used to build a lookup table, as shown in Fig. 8.

4.3.3 Numerical Results

In order to prove the statistical significance and robustness of the optimised pressure derivative threshold values found before, a new set of simulations has been run in MATLAB® Simulink, using a simulation time span of 800 times T_e (instead of 400) and different wave profiles characterized by the same statistical parameters (H_s and T_e). It must be mentioned that the power output values obtained in the optimisation simulations described in Sec. 4.3.2 differ from those obtained in the new set of simulations by less than 5% in average. This demonstrates the robustness of the identified values of $\dot{p}_{\text{th}}$.

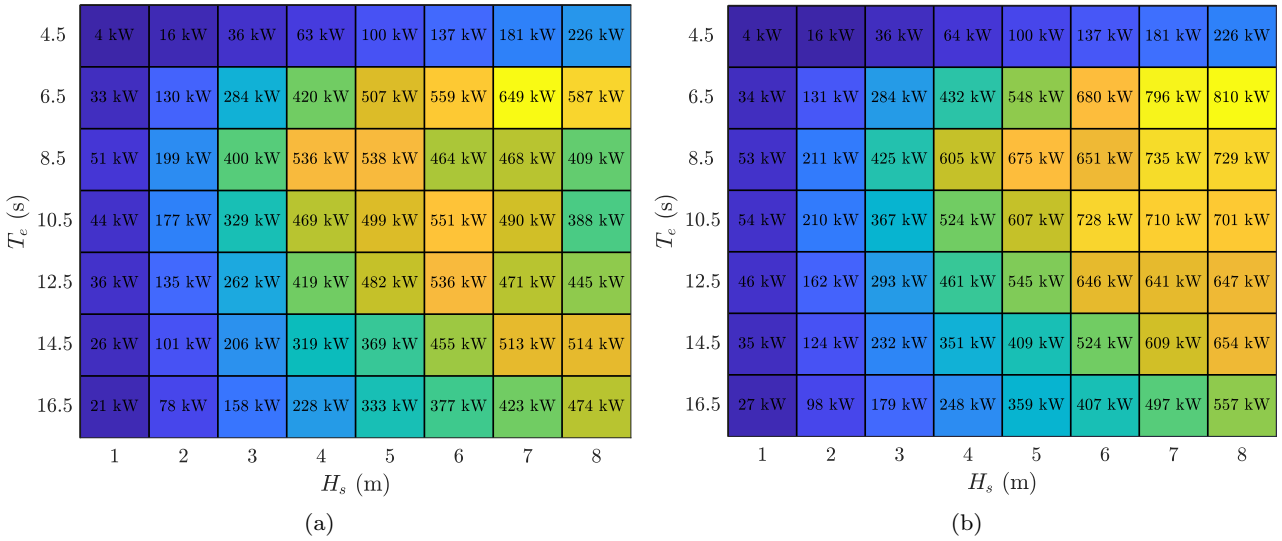

Fig. 9: Comparison of the power output as a function of the panchromatic wave parameters in the two cases of: (a) pressure derivative threshold equal to zero, (b) optimised pressure derivative threshold.

Figure 9 shows the power output results for the previously established control with pressure threshold equal to zero (see Fig. 9a) compared to the new optimised controller with tunable pressure threshold (Fig. 9b). In these matrices, results are shown for the whole set of considered sea states. Despite its simplicity, the new controller with tunable pressure derivative threshold provides an increased power output by more than 25% in most of the sea states.

In conclusion, although the proposed strategy does not represent the absolute optimal control for irregular waves (the determination of which would require complex online optimisations), it provides a significant improvement compared to previously established CD-DEG's control laws. It is expected that the improvement in performance would be even better if narrower spectral distributions were considered, as this would result in undisturbed wave profiles closer to the monochromatic case.

5 Conclusions

This paper addresses power maximisation and optimum control of an oscillating water column (OWC) wave energy converter (WEC) equipped with an inflatable dielectric elastomer generator (DEG) power take-off (PTO) system. The WEC is referred to as Poly-OWC.

We first propose a multi-physics model based on a linear description of the OWC hydrodynamics and on a non-linear electro-elastic model of the DEG. With reference to monochromatic sea states, we then propose a mathematical formulation for the problem of Poly-OWC's mean electric power maximisation in the presence of DEG topology and operational constraints. The proposed approach is based on an optimisation procedure performed in a steady-state periodic condition. The problem is formulated by discretising the relevant state variables and equations on a time horizon equal to the wave period, thus obtaining a quadratic objective function (namely, the electric energy generated by the device in a wave period) that depends on the discrete PTO's force time-history (which is the unknown variable of the optimisation problem). The electro-mechanical response of the DEG-PTO is used to define a set of constraints (namely, a feasible region) for the optimisation problem.

A case study is presented, in which the results obtained from the described optimisation in monochromatic waves are used to define a synthetic real-time control logic, solely based on the reading of a pressure sensor, the electro-mechanical parameters of the membrane, and the statistical information of the incoming waves. The deduced control logic is tested, in simulation, to the case of a Poly-OWC working in panchromatic waves. In particular, it is shown that, with a proper calibration of the control logics in presence of different sea states, an improvement up to 25% in power output can be obtained with respect to unoptimised control logics employed in previous works.

Future activities might include the experimental implementation of the proposed control heuristics through hardware-in-the-loop tests on ICD-DEGs samples or

experimental wave-tank tests on Poly-OWC prototypes.

6 Acknowledgements

The research leading to these results has received funding from the European Union Seventh Framework Programme [FP7/2007-2013], project PolyWEC, under grant agreement n 309139 and from the European Union Horizon 2020 program, project WETFEET, under grant No. 646436.

References

1. IPOPT. https://projects.coin-or.org/Ipopt (2016). Accessed: 2016-10-04
2. Opti toolbox. http://www.i2c2.aut.ac.nz/Wiki/OPTI/ (2016). Accessed: 2016-10-03
3. Babarit, A., Hals, J., Muliawan, M., Kurniawan, A., Moan, T., Krokstad, J.: Numerical benchmarking study of a selection of wave energy converters. Renewable Energy **41**, 44–63 (2012)
4. Camacho, E.F., Alba, C.B.: Model predictive control. Springer Science & Business Media (2013)
5. Carter, D.: Estimation of wave spectra from wave height and period (1982)
6. Chiba, S., Waki, M., Wada, T., Hirakawa, Y., Masuda, K., Ikoma, T.: Consistent ocean wave energy harvesting using electroactive polymer (dielectric elastomer) artificial muscle generators. Applied Energy **104**, 497–502 (2013)
7. Cretel, J.A., Lightbody, G., Thomas, G.P., Lewis, A.W.: Maximisation of energy capture by a wave-energy point absorber using model predictive control. IFAC Proceedings Volumes **44**(1), 3714–3721 (2011)
8. Cruz, J.: Ocean wave energy: current status and future prespectives. Springer Science & Business Media (2007)
9. Evans, D.: Maximum wave-power absorption under motion constraints. Applied Ocean Research **3**(4), 200–203 (1981)
10. Falcão, A.: Wave energy utilization: A review of the technologies. Renewable and sustainable energy reviews **14**(3), 899–918 (2010)
11. Falcão, A.d.O., De, O.: The shoreline OWC wave power plant at the Azores. In: Fourth European Wave Energy Conference, Aalborg, Denmark, pp. 4–6 (2000)
12. Falnes, J., et al.: Optimum control of oscillation of wave-energy converters. International Journal of Offshore and Polar Engineering **12**(02) (2002)
13. Fletcher, R., Leyffer, S., Toint, P.L.: On the global convergence of a filter–sqp algorithm. SIAM Journal on Optimization **13**(1), 44–59 (2002)
14. Hals, J., Falnes, J., Moan, T.: Constrained optimal control of a heaving buoy wave-energy converter. Journal of Offshore Mechanics and Arctic Engineering **133**(1), 011,401 (2011)
15. Halvorsen, E., Le, C., Mitcheson, P., Yeatman, E.: Architecture-independent power bound for vibration energy harvesters. In: Journal of Physics: Conference Series, vol. 476, p. 012026. IOP Publishing (2013)
16. Hamdi, A., Abdelaziz, M.N., Hocine, N.A., Heuillet, P., Benseddiq, N.: A fracture criterion of rubber-like materials under plane stress conditions. Polymer Testing **25**(8), 994–1005 (2006)
17. Henderson, R., Hunter, R.: Control requirements for wave energy converters. landscaping study. Tech. rep., Wave Energy Scotland (2016)
18. Henriques, J., Falcao, A., Gomes, R., Gato, L.: Latching control of an oscillating water column spar-buoy wave energy converter in regular waves. Journal of Offshore Mechanics and Arctic Engineering **135**(2), 021,902 (2013)
19. Horn, R.A.: The Hadamard product. In: Proc. Symp. Appl. Math, vol. 40, pp. 87–169 (1990)
20. Hosseinloo, A.H., Turitsyn, K.: Fundamental limits to nonlinear energy harvesting. Physical Review Applied **4**(6), 064,009 (2015)
21. Hudson, J., Phillips, D., Wilkins, N.: Materials aspects of wave energy converters. Journal of materials science **15**(6), 1337–1363 (1980)
22. Jean, P., Wattez, A., Ardoise, G., Melis, C., Van Kessel, R., Fourmon, A., Barrabino, E., Heemskerk, J., Queau, J.: Standing wave tube electro active polymer wave energy converter. In: SPIE Smart Structures and Materials+ Nondestructive Evaluation and Health Monitoring. International Society for Optics and Photonics (2012)
23. Kaltseis, R., Keplinger, C., Baumgartner, R., Kaltenbrunner, M., Li, T., Mächler, P., Schwödiauer, R., Suo, Z., Bauer, S.: Method for measuring energy generation and efficiency of dielectric elastomer generators. Applied Physics Letters **99**(16), 162,904 (2011)
24. Kaltseis, R., Keplinger, C., Koh, S.J.A., Baumgartner, R., Goh, Y.F., Ng, W.H., Kogler, A., Tröls, A., Foo, C.C., Suo, Z., et al.: Natural rubber for sustainable high-power electrical energy generation. RSC Advances **4**(53), 27,905–27,913 (2014)
25. Koh, S.J.A., Keplinger, C., Li, T., Bauer, S., Suo, Z.: Dielectric elastomer generators: how much energy can be converted? IEEE/ASME Transactions

on mechatronics **16**(1), 33–41 (2011)
26. Koh, S.J.A., Zhao, X., Suo, Z.: Maximal energy that can be converted by a dielectric elastomer generator. Applied Physics Letters **94**(26), 262,902 (2009)
27. Lee, C.H., Newman, J.N.: Wamit user manual. WAMIT, Inc (2006)
28. Mehrotra, S.: On the implementation of a primal-dual interior point method. SIAM Journal on optimization **2**(4), 575–601 (1992)
29. Moretti, G., Fontana, M., Vertechy, R.: Model-based design and optimization of a dielectric elastomer power take-off for oscillating wave surge energy converters. Meccanica **50**(11), 2797–2813 (2015)
30. Moretti, G., Rosati Papini, G.P., Alves, M., Grases, M., Vertechy, R., Fontana, M.: Analysis And Design of an Oscillating Water Column Wave Energy Converter with Dielectric Elastomer Power Take-Off. In: ASME 2015 34th International Conference on Ocean, Offshore and Arctic Engineering. American Society of Mechanical Engineers (2015)
31. Moretti, G., Rosati Papini, G.P., Fontana, M., Vertechy, R.: Hardware in the loop simulation of a dielectric elastomer generator for oscillating water column wave energy converters. In: OCEANS 2015-Genova, pp. 1–7. IEEE (2015)
32. Mørk, G., Barstow, S., Kabuth, A., Pontes, M.T.: Assessing the global wave energy potential. In: ASME 2010 29th International Conference on Ocean, Offshore and Arctic Engineering, pp. 447–454. American Society of Mechanical Engineers (2010)
33. Pelrine, R., Kornbluh, R.D., Eckerle, J., Jeuck, P., Oh, S., Pei, Q., Stanford, S.: Dielectric elastomers: generator mode fundamentals and applications. In: SPIE's 8th Annual International Symposium on Smart Structures and Materials, pp. 148–156. International Society for Optics and Photonics (2001)
34. Rossiter, J.A.: Model-based predictive control: a practical approach. CRC press (2003)
35. Scherber, B., Grauer, M., Kllnberger, A.: Electroactive polymers for gaining sea power (2013). DOI 10.1117/12.2009113
36. Teillant, M., Papini, G.R., Moretti, G., Vertechy, R., Fontana, M., Monkand, K., Alves, M.: Techno-economic comparison between air turbines and dielectric elastomer generators as power take off for oscillating water column wave energy converters. In: 11th European Wave & Tidal Energy Conference. Nantes, France (2015)
37. Tóth, R., Felici, F., Heuberger, P., Van den Hof, P.: Crucial aspects of zero-order hold lpv state-space system discretization. IFAC Proceedings Volumes **41**(2), 4952–4957 (2008)
38. Tröls, A., Kogler, A., Baumgartner, R., Kaltseis, R., Keplinger, C., Schwödiauer, R., Graz, I., Bauer, S.: Stretch dependence of the electrical breakdown strength and dielectric constant of dielectric elastomers. Smart Materials and Structures **22**(10), 104,012 (2013)
39. Vertechy, R., Fontana, M., Papini, G.R., Bergamasco, M.: Oscillating-water-column wave-energy-converter based on dielectric elastomer generator. In: SPIE Smart Structures and Materials+ Nondestructive Evaluation and Health Monitoring, pp. 86,870I–86,870I. International Society for Optics and Photonics (2013)
40. Vertechy, R., Fontana, M., Papini, G.R., Forehand, D.: In-tank tests of a dielectric elastomer generator for wave energy harvesting. In: SPIE Smart Structures and Materials+ Nondestructive Evaluation and Health Monitoring, pp. 90,561G–90,561G. International Society for Optics and Photonics (2014)
41. Vertechy, R., Fontana, M., Stiubianu, G., Cazacu, M.: Open-access dielectric elastomer material database. In: SPIE Smart Structures and Materials+ Nondestructive Evaluation and Health Monitoring. International Society for Optics and Photonics (2014)
42. Vertechy, R., Frisoli, A., Bergamasco, M., Carpi, F., Frediani, G., De Rossi, D.: Modeling and experimental validation of buckling dielectric elastomer actuators. Smart Materials and Structures **21**(9), 094,005 (2012)
43. Vertechy, R., Rosati Papini, G.P., Fontana, M.: Reduced model and application of inflating circular diaphragm dielectric elastomer generators for wave energy harvesting. Journal of Vibration and Acoustics **137**(1), 011,004 (2015)
44. Yu, Z., Falnes, J.: State-space modelling of a vertical cylinder in heave. Applied Ocean Research **17**(5), 265–275 (1995)

Physical constants		
Symbol	Unit	Description
g	m/s^2	Acceleration of gravity
P_{atm}	Pa	Atmospheric pressure
γ		Air's heat capacity ratio
ρ_w	kg/m^3	Sea water density
Hydrodynamic model (continuous time)		
Symbol	Unit	Description
$a,\ b,\ c,\ d$	m	OWC collector dimensions
A_j	m	$j-$th amplitude of irregular waves harmonic components
$\boldsymbol{A_r},\ \boldsymbol{B_r},\ \boldsymbol{C_r}$		Radiation state-space model matrices
$\boldsymbol{A_c},\ \boldsymbol{B_c},\ \boldsymbol{C_c}$		Hydrodynamic state-space model matrices
$\mathcal{E}_a$	J	Energy absorbed by the PTO machinery
f	N	PTO force
f_e	N	Excitation force
$f_{\text{MAX}},\ f_{\text{MIN}}$	N	Upper and lower envelopes of the PTO force profiles
H	m	Regular wave height
H_s	m	Significant irregular wave height
k_r	N/m	Radiation force kernel
m_∞	kg	Added mass at infinite frequency
n		Dimension of $\boldsymbol{x_c}$
p	Pa	Air chamber relative pressure
$\dot{p}_{th}$	Pa/s	Pressure derivative threshold
r		Dimension of $\boldsymbol{x_r}$
S	m^2	Water column cross-section
$S_\omega(\omega)$	m^{2}s	Wave spectrum
T	s	Regular wave period
T_e	s	Irregular wave energy period
u_c	m/s^2	State-space hydrodynamic model input
$\boldsymbol{x_c}$		Hydrodynamic model state vector
$\boldsymbol{x_r}$		Radiation state vector
$\hat{\Gamma}(\omega)$	N/m	Wave excitation coefficient
$\Delta\omega$	rad/s	step between consecutive values of ω_j
δ		Sign of the air pressure time derivative
η	m	Water column displacement
τ	s	Time
ϕ_j	rad	$j-$th phase of irregular waves harmonic components
ω	rad/s	Angular frequency
ω_j	rad/s	$j-$th frequency of irregular waves harmonic components
Hydrodynamic model (discrete time)		
Symbol	Unit	Description
$\boldsymbol{A_d},\ \boldsymbol{B_d},\ \boldsymbol{C_d}$		Discretisation of $\boldsymbol{A_c},\ \boldsymbol{B_c},\ \boldsymbol{C_c}$
N		Number of samples in a discretised horizon
$\boldsymbol{P},\ \boldsymbol{V}$		Matrices to extract velocity and water column displacement from $\boldsymbol{x_d}$
T_s	s	Discretisation time-step
u_d	m/s^2	Discretisation of u_c
$\boldsymbol{X},\ \boldsymbol{Z}$		Sparse matrices defined in Eq. (36)
$\boldsymbol{x_d}$		Discretisation of $\boldsymbol{x_c}$
$\boldsymbol{\Phi}$		Prediction system matrix
$\boldsymbol{\Gamma}$		Prediction input matrix
$\boldsymbol{\Upsilon}$		Matrix used to formulate the terminal state constraint

$\boldsymbol{\Omega_P},\ \boldsymbol{\Omega_V}$		Matrices that correlate the vectors of velocity and position to the input vector
ICD-DEG model		
Symbol	Unit	Description
C	F	Capacitance
E	V/m	Electric field at the tip element
E_{BD}	V/m	Break-down electric field
$\mathcal{E}_e$	J	Electrical energy supplied by the DEG
e	m	Flat DEG pre-stretched radius
e_0	m	DEG unstretched radius
h	m	Tip displacement
$h_{MAX},\ h_{MIN}$	m	Maximum and minimum admissible tip displacements
I	A	Current
I_{MAX}	A	Maximum admissible current
I_1		Gent invariant parameter
k_1	Pa	Gent stiffness parameter
n_l		Number of in-parallel layers
Q	C	Charge
R	m	ICD-DEG curvature
t	m	Flat DEG pre-stretched thickness
t_0	m	DEG unstretched thickness
V	V	Voltage
ϵ	F/m	Dielectric constant
ζ		Ratio of generated energy (per cycle) over maximum cyclic convertible energy
λ		Stretch at the tip element
$\lambda_1,\ \lambda_2$		Meridian and circumferential stretches
λ_p		Pre-stretch
λ_u		Rupture stretch
σ	Pa	Stress at the tip element
Ω	m^3	Current air chamber volume
Ω_d	m^3	Volume subtended by the ICD-DEG
Operators and notation		
Operator		Description
$\mathbf{0}_{\boldsymbol{a\times b}}$		Matrix of zeros with a rows and b columns
$\mathbf{1}_{\boldsymbol{a\times b}}$		Matrix of ones $\in \mathbb{R}^{a\times b}$
$\boldsymbol{I_a}$		Identity matrix of size a
$\dot{\xi}$		Time derivative of the generic variable ξ.
$\boldsymbol{\xi}^T$		The transposed of generic vector $\boldsymbol{\xi}$
ξ_{200}		Value/profile of generic variable ξ in the presence of maximum current constraint $I_{\mathrm{MAX}} = 200$ A
$\underset{i\to j}{\boldsymbol{\xi}}$		Short form for $\left(\boldsymbol{\xi}^T[i], \boldsymbol{\xi}^T[i+1], \ldots, \boldsymbol{\xi}^T[j]\right)^T$
$\underline{\boldsymbol{\xi}}$		Short form for $\underset{0\to N-1}{\boldsymbol{\xi}}$

Table 2: List of symbols.